Acta Biomaterialia xxx (2009) xxx–xxx

Contents lists available at ScienceDirect

Acta Biomaterialia

journal homepage: www.elsevier.com/locate/actabiomat

Improving the osteointegration and bone–implant interface by incorporation of bioactive particles in sol–gel coatings of stainless steel implants

Josefina Ballarre [a,b,*], Inderchand Manjubala [b], Wido H. Schreiner [c], Juan Carlos Orellano [d], Peter Fratzl [b], Silvia Ceré [a]

[a] INTEMA, Universidad Nacional del Mar del Plata – CONICET, Juan B. Justo 4302.B7608FDQ, Mar del Plata, Argentina
[b] Max Planck Institute of Colloids and Interfaces, Department of Biomaterials, 14476 Potsdam, Germany
[c] LSI-LANSEN, Departamento de Física, UFPR, CP 19081, 81531-990 Curitiba, Brazil
[d] Traumatología y Ortopedia, Hospital Interzonal General de Agudos "Oscar Alende", Mar del Plata, Argentina

ARTICLE INFO

Article history:
Received 11 June 2009
Received in revised form 7 September 2009
Accepted 9 October 2009
Available online xxxx

Keywords:
Coatings
Surgical grade stainless steel
Hydroxyapatite
Newly formed bone
SAXS

ABSTRACT

In this study, we report a hybrid organic–inorganic TEOS–MTES (tetraethylorthosilicate–methyltriethoxysilane) sol–gel-made coating as a potential solution to improve the in vivo performance of AISI 316L stainless steel, which is used as permanent bone implant material. These coatings act as barriers for ion migration, promoting the bioactivity of the implant surface. The addition of SiO_2 colloidal particles to the TEOS–MTES sol (10 or 30 mol.%) leads to thicker films and also acts as a film reinforcement. Also, the addition of bioactive glass–ceramic particles is considered responsible for enhancing osseointegration. In vitro assays for bioactivity in simulated body fluid showed the presence of crystalline hydroxyapatite (HA) crystals on the surface of the double coating with 10 mol.% SiO_2 samples on stainless steel after 30 days of immersion. The HA crystal lattice parameters are slightly different from stoichiometric HA. In vivo implantation experiments were carried out in a rat model to observe the osteointegration of the coated implants. The coatings promote the development of newly formed bone in the periphery of the implant, in both the remodellation zone and the marrow zone. The quality of the newly formed bone was assessed for mechanical and structural integrity by nanoindentation and small-angle X-ray scattering experiments. The different amount of colloidal silica present in the inner layer of the coating slightly affects the material quality of the newly formed bone but the nanoindentation results reveal that the lower amount of silica in the coating leads to mechanical properties similar to cortical bone.

1. Introduction

Metallic materials have found wide application as orthopedic devices as either permanent or temporary devices. When the orthopedic device has to remain permanently in the body, the bonding between the implant and the living tissue deserves attention. Alloys used for implants have in common their excellent mechanical properties in load-bearing sites. These metallic alloys have in common a high corrosion resistance in physiological media mainly due to the formation of a passive oxide film that reduces the corrosion rate by blocking the transport of metallic ions and electrons. Surface characterization of these metallic alloys is highly important as it is a tool to evaluate the performance of the implant through the surface film–tissue interaction and the possible migration of metallic ions from the base metal to the nearby tissue [1–7].

One of the ways of minimizing corrosion products which might release from the implant to the surrounding tissue consists in applying a protective biocompatible coating. Sol–gel coating has been proposed as an adequate method to achieve protective biocompatible films [8–12]. It has been demonstrated that inorganic-hybrid SiO_2 coatings, obtained from tetraethylorthosilicate (TEOS) and methyltriethoxysilane (MTES) in acidic catalysis, improve the corrosion behaviour of the AISI 316L stainless steel in biological environments [13,14]. Silica is also known as a natural catalyst for hydroxyapatite formation (HA: $Ca_{10}(PO_4)_6(OH)_2$), showing the bioactivity in vitro [15]. The in vitro deposited HA has been widely studied with microscopic, diffraction or spectroscopic techniques [16]. The addition of silica nanoparticles improves the coating thickness and enhances the attachment of glass–ceramic (GC) bioactive particles to them.

The extensive use of titanium and its alloys with chemical and mechanical surface treatments for permanent implants is supported by some osteoconductive and osteoinductive behaviour of these surfaces [17,18]. The use of stainless steel 316L for surgical permanent prostheses with the presence of a natural apatite depo-

* Corresponding author. Address: INTEMA, Corrosion Division, Universidad Nacional del Mar del Plata – CONICET, Juan B. Justo 4302.B7608FDQ, Mar del Plata, Argentina. Tel.: +54 223 4816600; fax: +54 223 4810046.
E-mail address: jballarre@fi.mdp.edu.ar (J. Ballarre).

1742-7061/$ - see front matter © 2009 Acta Materialia Inc. Published by Elsevier Ltd. All rights reserved.
doi:10.1016/j.actbio.2009.10.015

sition on the surface seems to be very difficult, due to the need for high concentrate and dense HAp or A/W coatings [19,20]. The catalytic effect of Si–OH group and Ti–OH groups for the apatite nucleation has been proven to form apatite in silica and titania gels immersed in simulated body fluid (SBF) [21].

The analysis of in vivo formation of new tissue at the interfaces of bioactive implants has been reported using histological methods and the interfacial mechanical properties, such as stiffness, have also been studied [22,23]. Recently other techniques that focus at the micro- and nano-structural level analysis of the newly formed tissue, such as nanoindentation, small-angle and wide-angle X-ray scattering, Raman microscopy and elemental analysis are being used in the analysis of biological materials [24,25]. These methods allow one to characterize the quality of the newly formed bone in terms of mechanical, structural and compositional analysis. Particularly, the small-angle X-ray scattering technique (SAXS) gives information about the mineral thickness, shape, orientation and arrangement within the complex collagen/mineral composite in bone [26,27].

This work proposes the protection of 316L stainless steel used as permanent implant material. Although stainless steel is seldom used in developed countries as permanent implants, it is still the most used in emerging countries. Hybrid TEOS–MTES–SiO_2 coating by sol–gel technique is applied onto the alloy in order to act as a barrier to ion diffusion to potentially toxic ions. SiO_2 colloidal particles were added to the sol function as reinforcement to the coating, giving additional protection to the aggressive environments. In vitro and in vivo studies of the bone–implant interfaces and the newly formed bone layers were carried out by evaluating HA formation, crystal structural parameters and mechanical strength of the newly formed tissue at the interface to the implant and the remodelled bone tissue in its vicinity.

2. Materials and methods

2.1. Materials

Stainless steel AISI 316L (Atlantic Stainless Co., Inc., MA, USA) in the form of sheets of 5×10 cm^2 and wires of 1.3 mm diameter and 2 cm length were used as substrates. The composition of the steel: C 0.03% max, Mn 2% max, Si 1% max, P 0.045% max, S 0.03% max, Ni 10–14%, Cr 16–18%, Mo 2–3%, balance Fe. They were degreased, washed with distilled water, and rinsed in ethanol before coating.

2.1.1. Preparation of the coating sols

Hybrid organic–inorganic sols were prepared with a silicon tetraethylorthosilane (TEOS, 99%, ABCR GmbH & Co., Germany), methyltriethoxysilane (MTES, 98%, ABCR GmbH & Co., Germany) and a water-based solution with colloidal silica (LEVASIL 200A 40 wt.%, Bayer, Germany). The molar ratio of the silanes were maintained constant (TEOS/MTES = 40/60) and the concentration of colloidal silica was varied between 10 and 30 mol.% with respect to the total amount of silica, and nitric acid (0.1 mol l^{-1}) was used as catalyser. The final silica concentration for both sols was 4.16 mol l^{-1}.

2.1.2. Glass–ceramic (GC) particles and suspension

The glass–ceramic particles were made from a precursor glass system SiO_2–P_2O_5–CaO. Silica sand (source), calcium carbonate (Aldrich) and orthophosphoric acid (Aldrich) were used as precursors. The ratio of components was calculated in order to obtain the weight concentration of CaO 47.29%, SiO_2 35.69% and P_2O_5 17.01% in the final glass. The mixture was fused in a platinum crucible at 1600 °C in air atmosphere, and then quenched in water. The thermal treatment of glass was made at 1050 °C for 2 h in an electric furnace with the aim of obtaining apatite and wollastonite as crystalline phases. The GC obtained was milled in an agate planetary mill (Fritsch Pulverisette, Germany), at a rotation speed of 1500 rpm for 4 h and the powder was sieved with Tyler screens (grades 270, 325 and 600) to obtain a diameter size distribution of less than 20 μm. The particle suspensions were prepared by adding 10 wt.% of GC particles to the TEOS–MTES–10% SiO_2 sol. The suspensions were stirred by a high shear mixing in a rotor–stator agitator (Silverson L2R, UK) for 6 min and 15 wt.% of solid surfactant was added [28].

2.1.3. Coating

All the samples were prepared as a double layer system. A first layer prepared with TEOS–MTES–SiO_2 sol was obtained at room temperature by dip-coating at a withdrawal rate of 25 cm min^{-1} or 18 cm min^{-1} for 10% and 30% of colloidal silica, respectively, dried at room temperature for 30 min, and heat treated for 30 min at 450 °C in an electric furnace. A second layer was made applying TEOS–MTES–10% SiO_2 with 10 wt.% GC particles on the top of the first one. The withdrawal and thermal treatment conditions used were the same as in the first layer. The dual coating systems are named as follows: C10 corresponds to TEOS–MTES–10% SiO_2 + TEOS–MTES–10% SiO_2 with 10% GC coatings, and C30 corresponds to TEOS–MTES–30% SiO_2 + TEOS–MTES–10% SiO_2 with 10% GC coatings. A scheme of coating deposition is shown in Fig. 1.

2.2. In vitro bioactivity analysis

Bioactivity of coated stainless steel substrates was analysed with immersion in SBF solution. SBF was prepared according the following chemical composition [29]: NaCl (8.053 g l^{-1}), KCl (0.224 g l^{-1}), $CaCl_2$ (0.278 g l^{-1}), $MgCl_2.6H_2O$ (0.305 g l^{-1}), K_2HPO_4 (0.174 g l^{-1}), $NaHCO_3$ (0.353 g l^{-1}), $(CH_2OH)_3$ CNH_2 (6.057 g l^{-1}). Concentrated hydrochloric acid (HCl) was added to adjust the pH to 7.25 ± 0.05. The samples were immersed in SBF for 30 days, and maintained at 37 °C in a sterilized oven.

2.2.1. X-ray photoelectron scattering (XPS) analysis

XPS assays of the SBF immersed samples were made with an ESCA 3000 system (Microtech, UK) with a chamber pressure lower than 10^{-9} mbar. The spectra were collected using MgK_α (1253.6 eV) radiation and the overall energy resolution was about 0.8 eV. Four samples were measured after 30 min of Ar^+ sputtering performed with an argon ion gun under an accelerating voltage of 3 kV without showing a significant deviation from one to each other. Survey spectra were recorded for the samples in the 0–1100 eV kinetic energy range by 1 eV steps. High-resolution scans with 0.1 eV steps were recorded over the following regions of interest: Fe 2p (706–712 eV), O 1s (525–534 eV), Ca 2p (345–349 eV) and P 2p (129.5–136 eV). The surface charging effects were compensated by referencing the binding energy (BE) to the C 1s line of residual carbon at 284.5 eV [30]. Data analysis was performed by a least squares fitting program (XPS XI-SDP Spectral Data Processor v2.3) and by fitting the spectral decomposition using mixed Gaussian–Lorenzian curves.

2.2.2. Wide-angle X-ray scattering (WAXS) analysis

To characterize the phase composition of the apatite coating formed in vitro, wide-angle X-ray scattering experiments were performed. The powder from the surface of the substrates, with and without immersion in SBF for 30 days, was gently scratched and collected on a glass substrate. The spectra were done using a powder diffractometer (D8 X-ray diffractometer, BruckerAXS, Meadowside, UK) with sealed tube and 1D 120° detector (Nonius).

Please cite this article in press as: Ballarre J et al. Improving the osteointegration and bone–implant interface by incorporation of bioactive particles in sol–gel coatings of stainless steel implants. Acta Biomater (2009), doi:10.1016/j.actbio.2009.10.015

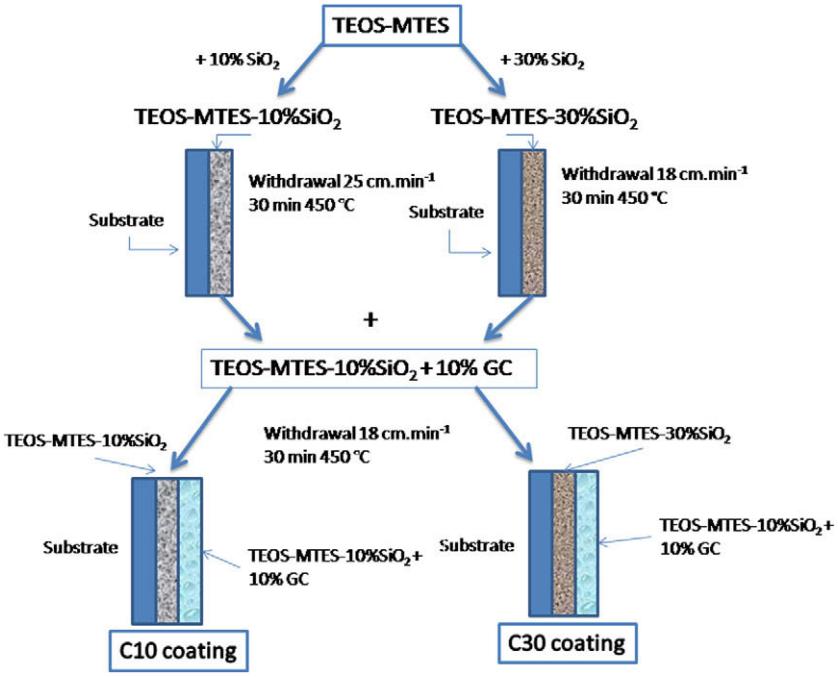

Fig. 1. Graphic scheme of the coating procedure on AISI 316 stainless steel substrates.

Analysing the diffractogram, the average crystallite size of the HA crystals grown in vitro were calculated from Scherrer's formula [31] using the equation,

$$L = K\lambda/\beta\cos\theta \quad (1)$$

where L is the average length of the crystal, λ the wavelength of CuK_α radiation (0.154178 nm), K is a constant related with the crystallite shape (0.9), θ is the diffraction angle (radians) and β is the full width of the peak at half of maximum intensity (radians). The diffraction peak at $\theta = 26.04°$ assigned to (0 0 2) plane was chosen for calculation of the crystallite length since it is isolated from others and represents the crystal size of the HA lattice in the c-axis direction. The broadening of the peaks, β, is corrected for instrumental broadening effects as follows:

$$\beta^2 = \beta^{*2} + \beta^2_{instr} \quad (2)$$

where β^* represents the HA crystallite contribution to the peak broadening while the β_{instr} is the instrumental broadening contribution. In this study, other lattice contributions were neglected [32]. The dimensions of the HA crystal lattice, a-axis and c-axis were calculated by considering all the peaks in the pattern that can be indexed using a MS-DOS basic program, assuming a hexagonal structure [33].

2.3. In vivo experiments and analysis

2.3.1. Implantation

In vivo experiments were conducted in total in six Hokkaido adult rats (weight 350 ± 50 g), according to rules of the ethical committee of the National University of Mar del Plata (Interdisciplinary Committee, April 2005), taking care of surgical procedures, pain control, standards of living and appropriated death. Coated and uncoated wires were sterilized in autoclave for 20 min at 121 °C. Rats were anaesthetized with fentanyl citrate and droperidol (Janssen-Cilag Lab, Johnson and Johnson, Madrid, Spain) according to their weight and the region of surgery surface was cleaned with antiseptic soap. The animals were placed in a supine position and the implantation site was exposed through the superior part of the tibia's internal face. A region of around 0.5 cm diameter was scraped in the tibia and femur plateau and a hole was drilled using a hand drill of 0.15 cm diameter bur at low speed. The implantation site was irrigated with physiological saline solution during the drilling procedure for cleaning and cooling proposes. The C10, C30 coated implants and uncoated wire implants, as controls, were placed by press fit into tibia and/or femur extending into the medullar canal. The animals were sacrificed with an overdose of intraperitoneal fentanyl citrate and droperidol after 60 days and the bone with implants was retrieved. Conventional X-ray radiographs were taken before retrieving the samples for control purposes.

2.3.2. Samples sectioning

The retrieved samples were cleaned from surrounding soft tissues and fixed in neutral 10 wt.% formaldehyde for 24 h. Then they were dehydrated in a series of acetone–water mixtures followed by a methacrylated solution and finally embedded in methyl methacrylate (PMMA) solution and polymerized. The PMMA embedded blocks were cut with a low speed diamond blade saw (Buehler GmbH) cooled with water. Various sections were made according to different analysis: 300–450 μm thick sections for SAXS measurements, 200 μm thick sections for histological staining, and 5 mm thick blocks for electron microscopy and nanoindentation studies. The samples used for nanoindentation were further polished with 120, 240, 400 and 600 grid paper lubricated with water and then fine polished with 3 μm alumina powder using an automatic grinding and polishing machine (Logitech, UK). Care was taken to keep the block surface free from scratches as much as possible.

2.3.3. Histological analysis and environmental scanning electron microscopy (ESEM)

The surface morphology of the implant–bone interface was observed with environmental scanning electron microscopy (ESEM Quanta 600 FEG) in low vacuum using a back-scattered electron (BSE) detector operated at 15 kV. The BSE images reveal the mineralized tissue regions and therefore lack the observation of the soft

Please cite this article in press as: Ballarre J et al. Improving the osteointegration and bone–implant interface by incorporation of bioactive particles in sol–gel coatings of stainless steel implants. Acta Biomater (2009), doi:10.1016/j.actbio.2009.10.015

tissue layer formed around the implant. To observe the soft tissue and the bone lining cells, the histological sections were stained with 20% Giemsa stain solution [34]. The stained sample sections were observed using an optical light microscope (Leica DM RXA2).

2.3.4. Nanoindentation measurements

The indentation modulus and hardness of the newly formed bone layer at the bone–implant interface were measured using a scanning nanoindenter (UB1, Hysitron, MN, USA), with a Berkovich diamond indenter. The high-resolution optical microscope attached to the piezo-scanner allows one to position the indenter tip precisely at the region of interest. The same indenter tip is also capable of making AFM images and thereby allows visualizing at high magnifications the region of interest and the indents made therein. The indenter tip was calibrated with fused silica. The regions for the measurements were pre-selected from ESEM-BSE images. In the bone–implant interface region, three lines of indents were scanned, each line consisting of eight indents at a spacing of 3 μm, with a maximum load of 1000 μN. Few indents were made in the cortical bone region for comparison. The contact stiffness (S) was calculated by an automated software that takes into account the slope only from 20% to 95% of the unloading curve. The hardness (H) and reduced modulus (E_r) were then calculated from the unloading contact stiffness, S, and the indenter contact area A_c based on the Oliver–Pharr theory [35,36] as

$$H = P_{max}/Ac$$
$$Er = \sqrt{\pi}S/2\sqrt{A}c \quad (3)$$

In this work, the reduced modulus is reported directly as the bone indentation modulus, without taking into account the Poisson's ratio of bone. The values of indentation modulus and hardness are reported as mean ± SD. The statistical significance between the newly formed bone and remodellation zone was performed by t-test using SigmaStat (SYSTAT Software Inc., Chicago, USA) with a significance threshold of $p < 0.05$.

2.3.5. Small-angle X-ray scattering analysis

SAXS samples were mounted on a sample holder perpendicular to the X-ray beam path and positioned using microcontrollers. Position-resolved measurements were enabled by a computer-controlled stage moving the sample in two directions (x and y). Before the measurements, radiography was performed by measuring the X-ray transmission rate of the sample with a diode setup and scanning the whole sample area with a step size of 0.2 mm. The SAXS measurement points were chosen from the radiography image, in the newly formed bone region at the periphery of the implant and a few points in the old cortex for comparison. The scanning SAXS measurements were performed using an instrument equipped with rotating Cu-anode generator operating at 12 kW, generating CuK_α radiation, wavelength 1.5419 Å, an evacuated double pinhole and a two-dimensional position-sensitive proportional counter detector (Siemens AG, Karlsruhe, Germany). The size of the X-ray beam was 200 μm at the sample and the sample-to-detector distance was about 60 cm. All the spectra were corrected for empty background scattering from the pinholes. The calibration of the beam centre position in the detector was done by measuring silver behanate (AgBh) sample. The reduction of SAXS pattern to obtain intensity data was done by Fit2D program (2-Dimensional Data Analyzer, ESRF, France), and further analysis for obtaining mineral particle thickness and orientation was done using a self-developed Pyton-based program.

The integration of the 2D SAXS data can be done either radially or azimuthally to obtain the mineral thickness (T-parameter) and the degree of alignment of the mineral particles (ρ-parameter). The predominant orientation can be calculated from the anisotropy of the SAXS pattern. The main direction of the long axis of the mineral particles and the width of their angular distribution (χ) can be obtained directly from the integration of $I(q,\chi)$ with respect to q. This leads to the resulting function $I(\chi)$ consisting of two peaks separated by 180°. The ρ-parameter, which is a measure for the portion of non-randomly oriented particles, is derived from dividing the area under the two peaks in $I(\chi)$ by the total area under the entire function. A value of $\rho = 0$ means that there is no predominant orientation and all particles are randomly oriented within the plane section, whereas $\rho = 1$ means that all particles are aligned along a predominant orientation. The mean thickness of the mineral particles is defined as:

$$T = 4\phi(1-\phi)/\sigma) \quad (4)$$

where ϕ is the total volume fraction of the mineral and σ is the total surface area of mineral particles per total tissue volume [26,27].

3. Results and discussion

3.1. Barrier effect

The hybrid organic–inorganic coatings applied by sol–gel method on surgical grade stainless steel were homogeneous and without evident defects or cracks on the surface, and they also presented good adherence and attachment to the metallic surface [37]. The average thickness of the coating, measured by profilometer, was 2.1 ± 0.2 μm and 2.3 ± 0.2 μm for the TEOS–MTES–SiO_2 10% and TEOS–MTES–SiO_2 30% single coating, respectively. The nanoparticles of SiO_2 added to reinforce the films filled the defects and holes present in the silica network, thereby decreasing the porosity and the conductivity of the surface [38].

XPS measurements were done in order to see the migration of metallic ions through the coatings. The "barrier effect" created by the coatings can be observed in Fig. 2 where results obtained for Fe, Cr and Ni elements are shown for both the coated samples after 30 days of immersion in SBF. There is no evidence of toxic elements like Cr and Ni in the surface of the in vitro samples after 30 days of immersion. Also it is important to note that Fe ions that migrated through TEOS–MTES films are somehow inhibited in the silica nanostructured coatings, since no evidence of Fe or Fe_2O_3 signal is present in the XPS high-resolution spectra [39]. The iron ions are smaller and more mobile than Cr and Ni and there is the most common cause of metalosis (necrosis of the tissues due to metallic ions) [3]. The inhibition of Fe in these coatings can be attributed either to the difference of thickness between the coatings (TEOS–MTES coating 1.6 μm, TEOS–MTES–SiO_2 10% single coating 2.1 μm and TEOS–MTES–SiO_2 30% single coating 2.3 μm) or to the accumulation and deposition of silicates at the metal-coating interface since the silica particles are more reactive at low alkaline pH than the silanols that formed the layer, covering flaws and existing defects [38].

3.2. In vitro apatite analysis

3.2.1. XPS analysis

The in vitro bioactivity of the implant was tested by studying the formation of bone-like apatite on the surface in SBF [40] by the measurement and quantification of the high-resolution spectra of the characteristic elements of apatite: Ca, P and O, for the C10 and C30 samples after 30 days of immersion in SBF. A glass–ceramic (GC) powder sample was also analysed for comparison with the initial quantity of Ca and P in the surface coating. By comparing the proportion of the peaks area, the relationships between Ca, O and P molar ratio were obtained. It was found that the value of Ca/P ratio for the GC particles was 3.86 whereas for the C10 sample

Please cite this article in press as: Ballarre J et al. Improving the osteointegration and bone–implant interface by incorporation of bioactive particles in sol–gel coatings of stainless steel implants. Acta Biomater (2009), doi:10.1016/j.actbio.2009.10.015

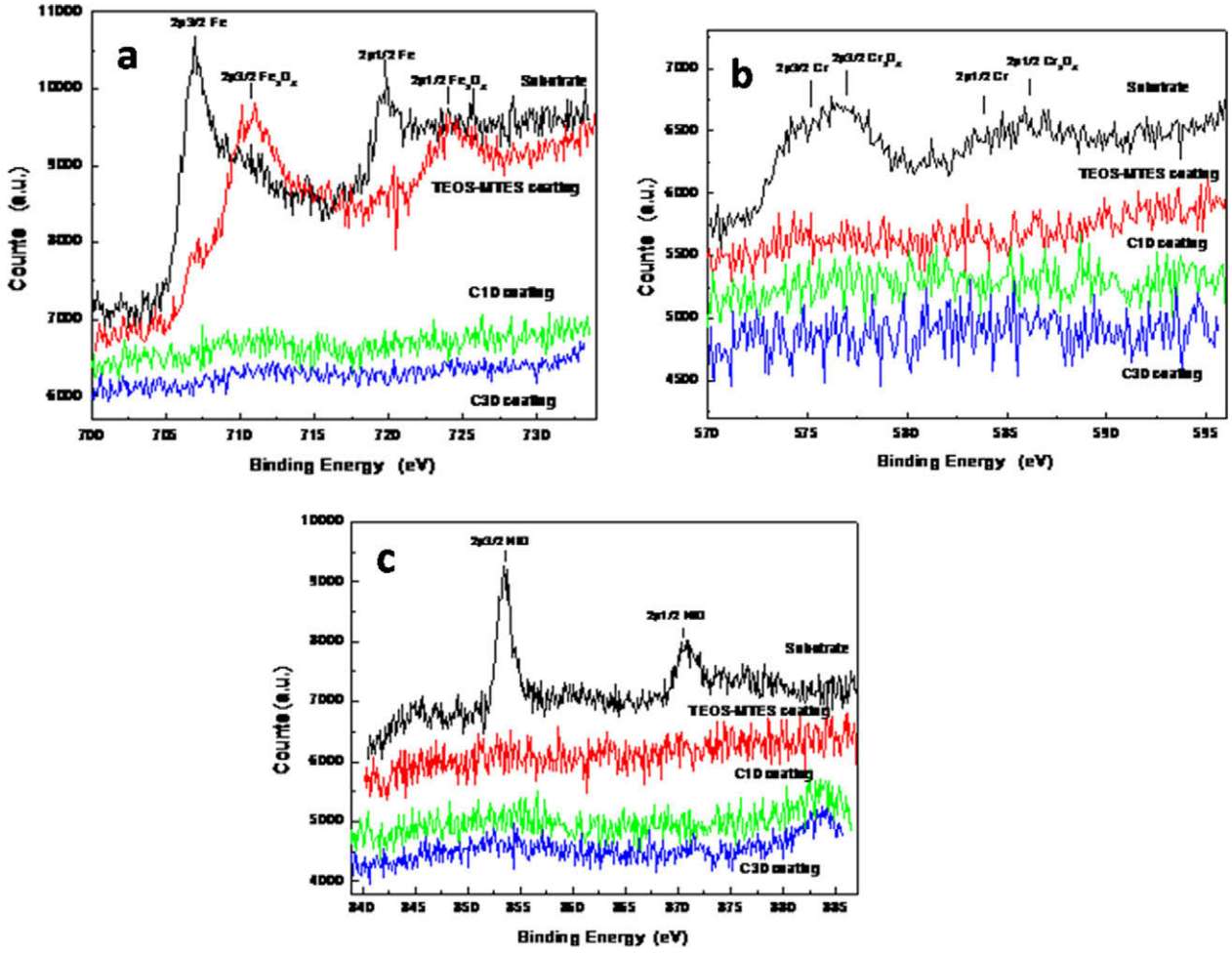

Fig. 2. High-resolution XPS scan of Fe2p (a), Cr2p (b) and Ni2p (c) for uncoated SS316L and coated with TEOS–MTES, coated with TEOS–MTES–$SiO_2$10% + TEOS–MTES–$SiO_2$10% with GC particles (C10) and coated with TEOS–MTES–$SiO_2$30% + TEOS–MTES–$SiO_2$10% with GC particles (C30) after immersion in simulated body fluid (SBF) for 1 day and 30 days.

immersed in SBF it was 1.43. The standard stoichiometric hydroxyapatite (HA) has a Ca/P ratio of 1.67 [41]. In addition, O/P and O/Ca ratio values for the C10 sample immersed in SBF were 4.13 and 2.88, slightly different from the stoichiometric HA that has values of 4.33 and 2.6, respectively. These values for GC bioactive particles are 3.86 and 3, respectively. The values obtained for C10 samples support the HA dissolution/redeposition theory conducted by Kokubo et al. [17], Peitl et al. [42] and Li et al. [43] which states the beginning of dissolution of glass–ceramic materials forming partially crystallized apatite (A) and wollastonite (W) phases, obtaining apatite-like deposits after immersion in SBF for a period of time. The deposition and formation mechanism of apatite-like layer and its composition depend largely on the substrate and the media content. The substrates in which the apatite layer is deposited can also be activated by adding functional groups that help in apatite nucleation. Therefore, the use of a silica-based coating supporting the GC particles is a way to improve the coating and increase the bioactivity of the stainless steel surfaces.

3.2.2. Wide-angle X-ray scattering analysis

Wide-angle X-ray scattering (WAXS) was done on the powders collected from C10 and C30 coatings on SS316L after 30 days of immersion in SBF as shown in Fig. 3. The powder sample from C30 coating without immersion in SBF was measured for comparison as shown in Fig. 3. There was no difference observed in the powders from C30 before and after immersion, suggesting there

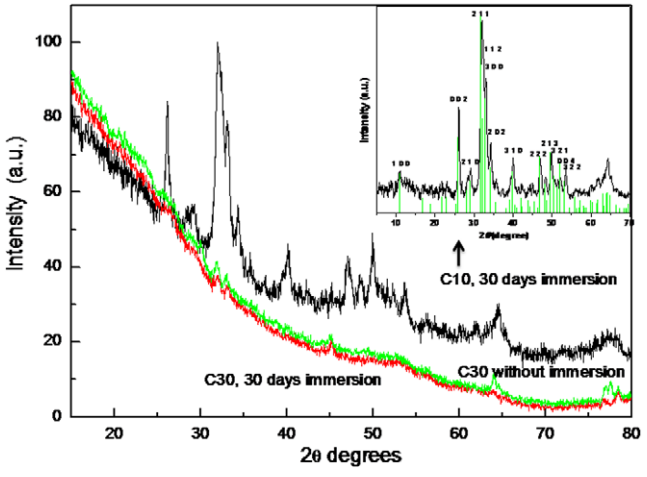

Fig. 3. (a) WAXS patterns for C10 and C30 samples after 30 days of immersion in SBF and C30 sample without immersion in SBF for comparison. (b) Enlarged view of the WAXS pattern of C10 with 30 days of immersion sample in the range 10–70° (2θ) comparing with standard JCPS 9-0432 pattern of HA (vertical lines).

was no formation of apatite layer in this sample. The powder from C10 sample shows highly crystalline peaks, corresponding to hydroxyapatite, and the enlargement of the spectrum for C10 after 30 days' immersion, after subtracting the background scattering, is

Please cite this article in press as: Ballarre J et al. Improving the osteointegration and bone–implant interface by incorporation of bioactive particles in sol–gel coatings of stainless steel implants. Acta Biomater (2009), doi:10.1016/j.actbio.2009.10.015

shown in the right upper graph in Fig. 3. The more intense peaks are indexed according to JCPDS 9-0432.

The indexed peaks of the C10 sample were used to calculate the lattice parameters "*a*-axis" and "*c*-axis" of HA crystal lattice. The obtained values of lattice parameters are listed in Table 1 in comparison with the standard HA (JCPDS 9-0432).

The small decrease in *c*-axis and the small increase of *a*-axis could indicate that the deposited apatite on the C10 sample after 30 days of immersion is slightly deformed due to the hydroxyl substitution by carbonates and to the Ca^{2+} substitution by other cations like Na^{+}, to keep the charge balance constant [44], leading to a non-stoichiometric HA [45]. The XPS results also confirmed the formation of non-stoichiometric HA.

The average crystallite size of the HA crystals growth in vitro, in the direction perpendicular to the crystallographic plane, was estimated from distinctive (0 0 2) and (3 1 0) peaks using Scherrer's formula. The average crystallite size of the HA crystals was calculated as L_{002} = 29.3 nm and L_{310} = 15.7 nm, which describes the size of crystal predominantly defined by *c*- and *a*-axes direction.

3.3. In vivo samples

3.3.1. Histology and scanning electron microscopy analysis

Fig. 4 shows the microscopic images of Giemsa stained sections of implanted C10 and C30 samples after 60 days of implantation in rat tibias. The remodellation zone between the implant and the old cortex bone is clearly visible (marked with arrow). The new lamellae bone tissue growth seems to be perpendicular to the longer axis of the nail-like implant, and perpendicular to the existing cortical bone. The formation of an osteoblastic-rich (osteoid layer) surface near the implant in C10 sample can be seen.

Table 1
Lattice parameters of hydroxyapatite formed during immersion in SBF for 30 days for C30 sample and comparing with the values found in JDPCS 9-0432.

	"*a*" parameter (Å)	"*c*" parameter (Å)
HAp (JCPDS 9-0432)	9.418	6.884
C10 with 30 days of immersion	9.449	6.791

The morphology of the cross-section of bone–implant interface as observed by ESEM is shown in Fig. 5a and b for the samples C10 and C30, respectively. The cross-section cut-level is approximately 15 mm away from the top of the epiphysis and still it is possible to observe that the implants were well positioned with 10–20% of their surface in contact with the old cortical bone and the remaining in contact with the bone marrow. The major difference between the C10 and C30 implant is that the new bone formed in the periphery of the implant surface of C30 is denser and appears to cover fully the implant surface when compared to C10 where the newly formed bone is not very dense and not continuous on the surface. Based on these images, the regions for nanoindentation measurements were selected as shown with white boxes. A position close to the old bone and a position near the marrow for each sample were chosen and an old cortex area was also measured for comparison as seen from Fig. 5c.

3.3.2. Nanoindentation analysis

Nanoindentation measurements were carried out in order to compare the stiffness and hardness of the newly formed bone at the bone–implant interface, which was in contact with the cortex old bone and medullar cavity. Fig. 6a shows a typical load–displacement curve of the indents made in the newly formed bone and old cortex bone. It illustrates the difference in penetration depth with the same applied load for the old cortical bone and for the newly formed less mineralized tissue. Also the morphology

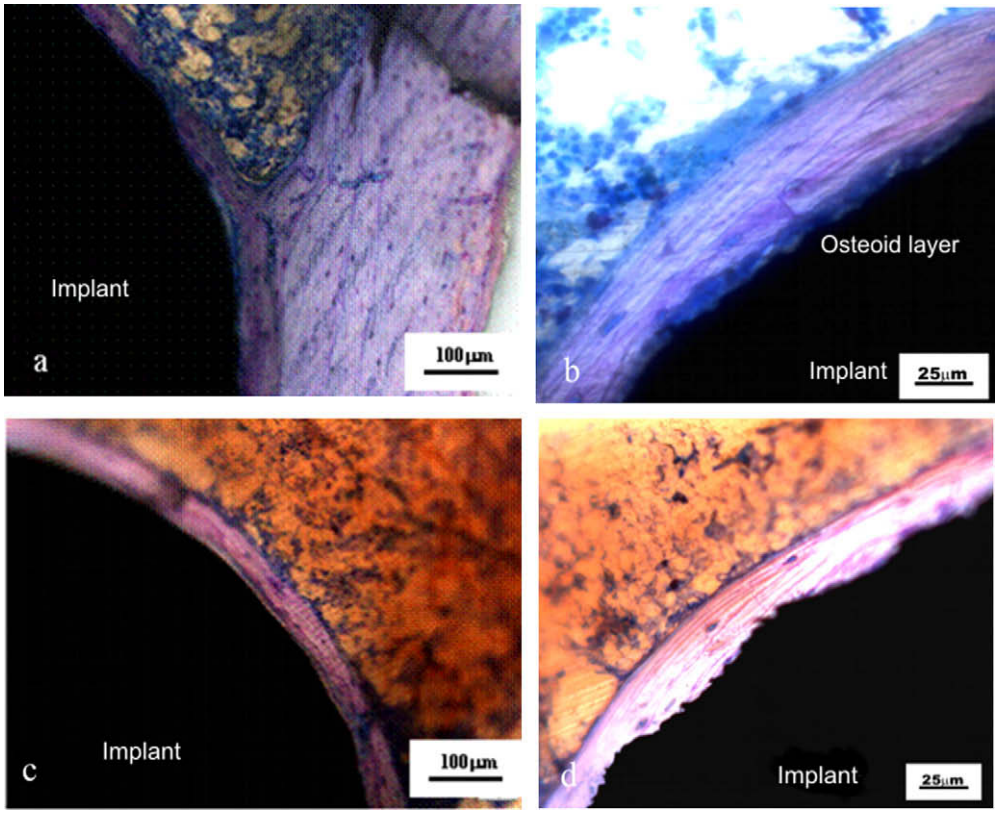

Fig. 4. Optical microscopic images of Giemsa stained histology sections showing the implant and the newly formed bone. (a and b) C10 sample and (c and d) C30 sample after 60 days of implantation in rat tibias. It can be observed that in sample C10 there is formation of osteoid layer around the implant which is not seen in sample C30.

Please cite this article in press as: Ballarre J et al. Improving the osteointegration and bone–implant interface by incorporation of bioactive particles in sol–gel coatings of stainless steel implants. Acta Biomater (2009), doi:10.1016/j.actbio.2009.10.015

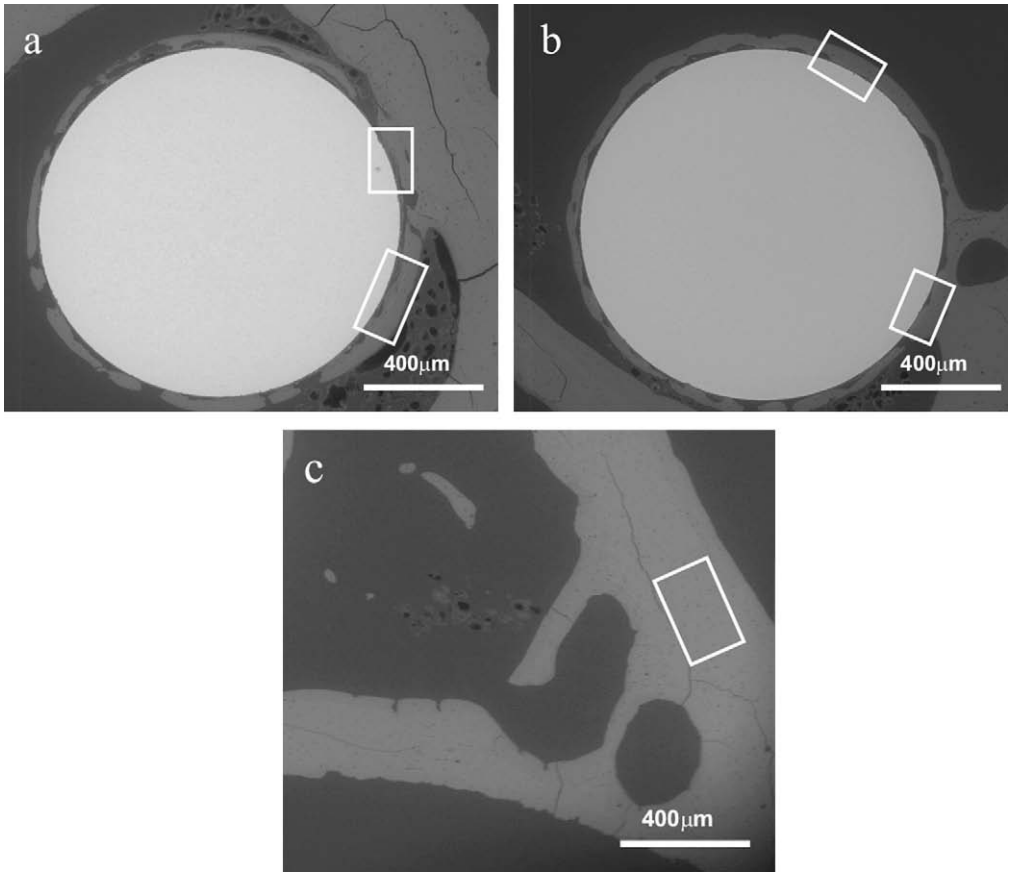

Fig. 5. ESEM images for overview cross-section (a) C10 and (b) C30 samples after 60 days of implantation. The regions for indentation measurements are marked with white squares to be in the newly formed bone around the implant, one being in contact with old cortical bone and the other being in contact with bone marrow. (c) The cortex region was chosen for comparison from the same sample.

of the indent: seen from the AFM image (Fig. 6b), the size of the indent in the old bone tissue is smaller than the one made in the remodellation zone for the C30 sample. The mean values of the indentation modulus and the hardness are listed in Table 2 for the regions of the new bone tissue formed near the marrow and of nearby old cortical bone for samples C10 and C30, respectively. In the C30 sample, the newly formed bone tissue in contact with the cortex (remodellation zone) is softer than the newly formed bone in the marrow region and the indentation modulus and hardness are much lower to the old cortical bone. This implies that the new bone in contact with the cortex also undergoes a remodelling process along with the cortical bone processes. It can be noted that the newly formed mineralized bone tissue along the periphery of the sample C10 after 60 days of implantation has similar elastic-mechanical properties compared to the old cortical bone. This indicates that the newly formed bone layer around the C10 implant is equivalent to a mature bone in terms of mechanical integrity.

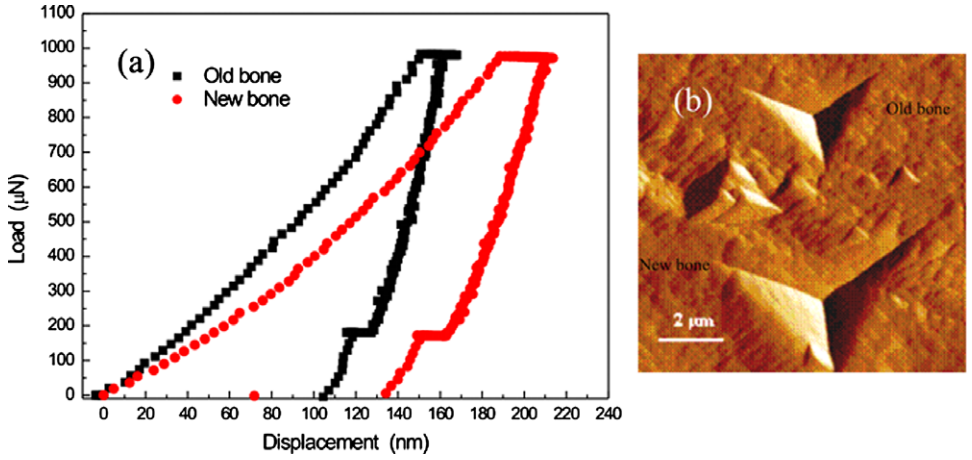

Fig. 6. (a) Load–displacement curves with 1000 μN maximum load on sample C30 in remodellation zone, showing clear differences in the displacement values and (b) an AFM image of the respective indents.

Please cite this article in press as: Ballarre J et al. Improving the osteointegration and bone–implant interface by incorporation of bioactive particles in sol–gel coatings of stainless steel implants. Acta Biomater (2009), doi:10.1016/j.actbio.2009.10.015

Table 2
Indentation modulus and hardness values in the regions of cortical, newly formed and remodelled bone for C10 and C30 samples.

	Indentation modulus GPa (mean ± SD)	Hardness GPa (mean ± SD)
Cortical bone	33.40 ± 2.79	1.64 ± 0.21
C10		
Remodellation zone	33.02 ± 4.20	1.47 ± 0.19
Marrow zone	33.26 ± 5.42	1.58 ± 0.30
C30		
Remodellation zone	18.55 ± 3.56	0.84 ± 0.15
Marrow zone	24.64 ± 4.16	1.01 ± 0.21

3.3.3. SAXS analysis

The scanning SAXS measurements were done in the newly formed region around the periphery of the implant and also in cortical bone for comparison. Table 3 gives the values of the mean mineral thickness (T) in the old cortical bone, in the remodellation zone (where the implant is in contact with the old bone tissue) and in the zone of newly formed bone (where the implant is just in contact with the marrow) for both C10 and C30 implants. The mineral particles are smaller in size in the newly formed bone compared to the old cortex. In both locations, near the cortex and near the marrow, comparing the same position for the samples C10 and C30, the values were not significantly different ($P < 0.001$ with t-test).

Fig. 7 shows the radiograph of the C10 and C30 samples after 60 days' implantation in rat tibias with a colour coding representing the X-ray transmission values through the sample. The orientation of the mineral particles in the measured spots of the newly formed bone is represented in the same figure with small black bars. The length of the bar denotes the degree of alignment of the particles (ρ-parameter) and the direction of the bar gives the overall preferred orientation of the mineral particles. Since the mineral particles (HA) are aligned with the longitudinal axis of the collagen fibrils, ρ gives also information about the orientation of this organic matrix. It can be seen that the newly formed bone around the C10 implant (Fig. 7a) has mineral crystals with preferential orientation parallel to the direction of the trabecular bone and follows the circumference of the implant. On the other hand, the mineral particles in the newly formed bone of the C30 implant are randomly oriented and are mostly perpendicular to the circumference of the implant (Fig. 7b). It is worth noting that in both samples, the mineral particles in the old cortex follow the architecture of the bone and are aligned to the direction of bone growth. These results are in agreement with the in vitro experiment where it was observed that the C30 coating did not produce an apatite layer whereas C10 formed crystalline apatite layer on the surface after immersion in SBF (Fig. 3a) and the histology analysis showed an osteoid-like layer for C10 sample. Also from the nanoindentation results, the newly formed bone in the C10 implant showed stiffness and hardness values similar to the old cortical bone, implying that the newly formed bone behaves as mature bone. The SAXS data also support the idea that the C10 implant results in well-organized bone structure (Fig. 7a), due to increased bioactivity at the surface.

These results indicate that the amount of silica nanoparticles plays a role in increasing the bioactivity of the coating in the metallic implants. A smaller amount of silica (10%) in the inner layer was found to be slightly better than 30% in the coatings. As the silica nanoparticles added to the silica-based hybrid coatings decrease the porosity, the denser the coatings become, as Montemor et al. had proved [38], and the nucleation site for apatite is blocked. As regards this relation between apatite formation and silica content, some related results were presented by Li et al. [21] showing the catalytic effect of Si–OH groups for the apatite nucleation that promote the formation of apatite in silica gels immersed in SBF. Also, Peitl et al. [42] pointed out that highly bioactive silica-based glasses and glass–ceramics materials promote apatite formation in vitro, but the in vivo formation with different amounts of silica nanoparticles is still under discussion and this work could be a starting point for that.

Table 3
T-parameter of the mineral crystals in bone after 60 days of implantation of samples C10 and C30 in rat tibia.

Region	Sample C10 (mean ± SD)	Sample C30 (mean ± SD)
Cortex	2.70 ± 0.04 nm	2.65 ± 0.18 nm
Remodellation zone	2.47 ± 0.02 nm	2.44 ± 0.21 nm
Marrow zone	2.29 ± 0.07 nm	2.41 ± 0.23 nm

4. Conclusions

The protection of surgical grade stainless steel implants against corrosion can be achieved by applying hybrid organic–inorganic sol–gel silica-based coatings. The addition of silica nanoparticles and glass–ceramic particles to the sol–gel coating enables the isolation of potentially toxic ions coming from the alloy to the surrounding environment. The in vitro bioactivity and implant–tissue

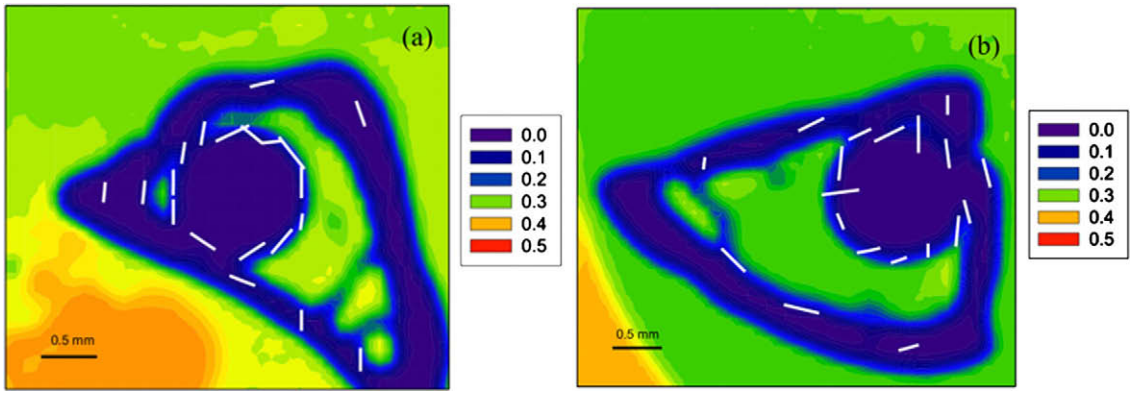

Fig. 7. Radiograph of the samples (a) C10 and (b) C30 samples after 60 days of implantation measured with SAXS showing the intensity of the transmitted X-ray through the sample section. The small white bars denote the degree of orientation of the mineral particles in the measured spots around the implant, the size of bar denotes the degree of alignment and the direction of the bars denotes the orientation of the mineral particles. It can be noted that the white bars are oriented along the implant surface in newly formed bone in C10 sample (a) and randomly distributed in C30 sample (b).

Please cite this article in press as: Ballarre J et al. Improving the osteointegration and bone–implant interface by incorporation of bioactive particles in sol–gel coatings of stainless steel implants. Acta Biomater (2009), doi:10.1016/j.actbio.2009.10.015

integration is promoted by the addition of such silica nanoparticles. The TEOS–MTES–SiO_2 with GC system coatings on stainless steel promotes the formation and growth of non-stoichiometric hydroxyapatite during in vitro tests when the amount of silica particles is less. The different amount of colloidal silica slightly affects the quality of the mineral crystals formed in the new bone in in vivo conditions. The stiffness of the newly formed bone in the implant with a lower amount of silica nanoparticles seems to be similar to the values for old cortex bone, showing short periods of maturation and mineralization of newly formed bone tissue around the implant.

Acknowledgements

The authors acknowledge the SeCyT-CAPES Cooperation program and the DuPont-CONICET award for financial support. The authors acknowledge Dr. Chenghao Li at MPI for his self-developed Pyton-based SAXS analysis program. J. Ballarre acknowledges the Deutsche Akademische Austauschdienst (DAAD) for award of exchange scholarship.

Appendix A. Figures with essential colour discrimination

Certain figures in this article, particularly Figs. 1–4, 6 and 7, are difficult to interpret in black and white. The full colour images can be found in the on-line version, at doi: 10.1016/j.actbio.2009.10.015).

References

[1] Doorn PF, Campbell PA, Worrall J, Benya PD, McKellop HA, Amstutz HC. Metal wear particle characterization from metal on metal total hip replacements: transmission electron microscopy study of periprosthetic tissues and isolated particles. J Biomed Mater Res 1998;42:103–11.
[2] Wintere G. Tissue reactions to metallic wear and corrosion products in human patients. J Biomed Mater Res Symp 1974;5:11–26.
[3] Bullen J, Rogers H, Spalding P, Ward C. Iron and infection, the heart of the matter. FEMS Immunol Med Microbiol 2005;43:325–30.
[4] Okazaki Y, Gotoh E, Manabe T, Kobayashi K. Comparison of metal concentrations in rat tibia tissues with various metallic implants. Biomaterials 2004;25:5913–20.
[5] Disegi JA, Eschbach L. Stainless steel in bone surgery. Injury Int J Care Injured 2000;31:S-D2–6.
[6] McGregor DB, Baan RA, Partensky C, Rice JM, Wilbourm JD. Evaluation of the carcinogenic risks to humans associated with surgical implants and other foreign bodies – a report of an IARC Monographs Programme Meeting. International Agency for Research on Cancer. Eur J Cancer 2000;36:307–13.
[7] López DA, Durán A, Ceré S. Electrochemical characterization of AISI 316L stainless steel in contact with simulated body fluid under infection conditions. J Mater Sci: Mater Med 2008;19(5):2137–44.
[8] de Sanctis O, Gómez L, Pellegri N, Parodi C, Marajofsky A, Durán A. Coatings on metallic substrates. J Non-Cryst Solids 1990;121:338–43.
[9] de Damborenea JJ, Pellegrini N, de Sanctis O, Durán A. Electrochemical behaviour of SiO_2 sol–gel coatings on stainless steel. J Sol–Gel Sci Technol 1995;4:239–44.
[10] Naderi Zand B, Mahdavian M. Evaluation of the effect of vinyltrimethoxysilane on corrosion resistance and adhesion strength of epoxy coated AA1050. Electrochim Acta 2007;52:6438–42.
[11] Castro Y, Ferrari B, Moreno R, Durán A. Corrosion behaviour of silica hybrid coatings produced from basic catalysed particulate sols by dipping and EPD. Surf Coat Technol 2005;191:228–35.
[12] Chou TP, Chandrasekaran C, Limmer SJ, Seraji S, Wu Y, Forbess MJ, et al. Organic–inorganic hybrid coatings for corrosion protection. J Non-Cryst Solids 2001;290:153–62.
[13] Galliano P, de Damborenea JJ, Pascual MJ, Durán A. Sol–gel coatings on 316L steel for clinical applications. J Sol–Gel Sci Technol 1998;13:723–7.
[14] Gallardo J, Galliano PG, Durán A. Bioactive and protective sol–gel coatings on metals for orthopaedic prosthesis. J Sol–Gel Sci Technol 2001;21:65–74.
[15] Li R, Clark AE, Hench LL. An investigation of bioactive glass powders by sol–gel processing. J Appl Biomater 1991;2(4):231–9.
[16] Fathi MH, Hanifi A, Mortazavi V. Preparation and bioactivity evaluation of bone-like hydroxyapatite nanopowder. J Mater Proc Technol 2008;202(1–3):536–42.
[17] Kokubo T, Kim H-M, Kawashita M. Novel bioactive materials with different mechanical properties. Biomaterials 2003;24:2161–75.
[18] Gu YW, Khor KA, Cheang P. In vitro studies of plasma-sprayed hydroxyapatite/Ti–6Al–4V composite coatings in simulated body fluid (SBF). Biomaterials 2003;24:1603–11.
[19] Lin F-H, Hsu Y-S, Lin S-H, Sun J-S. The effect of Ca/P concentration and temperature of simulated body fluid on the growth of hydroxyapatite coating on alkali-treated 316L stainless steel. Biomaterials 2002;23:4029–38.
[20] Liu X, Ding C, Chu PK. Mechanism of apatite formation on wollastonite coatings in simulated body fluid. Biomaterials 2004;25:1755–61.
[21] Li P, Ohtsuki C, Kokubo T, Nakanishi K, Soga N, Nakamura T, et al. Apatite formation induced on silica gel in a simulated body fluid. J Non-Cryst Solids 1992;75:2094–7.
[22] Gao T, Lindholm T, Kommonen B, Ragni P, Paranzini A, Lindholm TC, et al. Enhanced healing of segmental tibial defects in sheep by a composite bone substitute composed of tricalcium phosphate cylinder, bone morphogenetic protein, and Type IV collagen. J Biomed Mater Res 1996;32:505–12.
[23] Coathup M, Blunn G, Flynn N, Williams C, Thomas N. A comparison of bone remodelling around hydroxyapatite-coated, porous-coated and grit-blasted hip replacements retrieved at post-mortem. J Bone Joint Surg (Br) 2001;82B:118–23.
[24] Fratzl P, Gupta HS, Paschalis EP, Roschger P. Structure and mechanical quality of the collagen–mineral nano-composite in bone. J Mater Chem 2004;14:2115–23.
[25] Fratzl P, Weinkamer R. Nature's hierarchical materials. Prog Mater Sci 2007;52(8):1263–334.
[26] Fratzl P, Gupta H, Paris O, Valenta A, Roschger P, Klaushofer K. Diffracting stacks of cards – some thoughts about small-angle scattering from bone. Prog Colloid Polym Sci 2005;130:33–9.
[27] Fratzl P, Schreiber S, Klaushofer K. Bone mineralization as studied by small-angle X-ray scattering. Connect Tissue Res 1996;34(4):247–54.
[28] García C, Durán A, Moreno R. Stability of suspensions of bioactive particles using hybrid organic–inorganic solutions as dispersing media. J Sol–Gel Sci Technol 2005;34:1–7.
[29] Kokubo T, Kushitani H, Sakka S, Kitsugi T, Yamamuro T. Solutions able to reproduce in vivo surface-structure changes in bioactive glass–ceramic A–W. J Biomed Mater Res 1990;24:721–34.
[30] Moulder F, Stickle WF, Sobol PE, Bomben KD, editors. Handbook of X-ray photoelectron spectroscopy. Eden Praire, MN, USA: Physical Electronics, Inc.; 1995.
[31] Cullity BD, Stock SR. Elements of X-ray diffraction. NJ, USA: Prentice Hall; 2001.
[32] Rusu VM, Ng C-H, Wilke M, Tiersch B, Fratzl P, Peter MG. Size-controlled hydroxyapatite nanoparticles as self-organized organic–inorganic composite materials. Biomaterials 2005;26:5414–26.
[33] Manjubala I, Sampath Kumar TS. Effect of TiO_2–Ag_2O additives on the formation of calcium phosphate based functionally graded bioceramics. Biomaterials 2000;21:1995–2002.
[34] Bradbeer JN, Riminucci M, Bianco P. Giemsa as a fluorescent stain for mineralized bone. J Histochem Cytochem 1994;42(5):677–80.
[35] Oliver W, Pharr G. An improved technique for determining hardness and elastic-modulus using load and displacement sensing indentation experiments. J Mater Res 1992;7(6):1564–83.
[36] Oliver W, Pharr G. Measurement of hardness and elastic modulus by instrumented indentation: advances in understanding and refinements to methodology. J Mater Res 2004;19(1):3–20.
[37] Ballarre J, Jimenez-Piqué E, Anglada M, Pellice SA, Cavalieri AL. Mechanical characterization of nano-reinforced silica based sol–gel hybrid coatings on AISI 316L stainless steel using nanoindentation techniques. Surf Coat Technol 2009;203:3325–31.
[38] Montemor MF, Cabral AM, Zheludkevich ML, Ferreira MGS. The corrosion resistance of hot dip galvanized steel pretreated with Bis-functional silanes modified with microsilica. Surf Coat Technol 2006;200(9):2875–85.
[39] López DA, Rosero-Navarro NC, Ballarre J, Durán A, Aparicio M, Ceré S. Electrochemical evaluation of multilayer silica–methacrylate hybrid sol–gel coatings containing bioactive particles on surgical grade stainless steel. Surf Coat Technol 2008;202(10):2194–201.
[40] Kokubo T. A/W Glass-ceramic: processing and properties. In: Hench LL, Wilson J, editors. An introduction to bioceramics. World Scientific; 1993.
[41] Ballarre J, Pellice S, Scheiner W, Ceré S. Coatings containing silica nanoparticles and glass ceramic particles applied onto surgical grade stainless steel. Key Eng Mater 2009;396–398:311–4.
[42] Peitl O, Zanotto Dutra E, Hench LL. Highly bioactive P_2O_5–Na_2O–CaO–SiO_2 glass–ceramics. J Non-Cryst Solids 2001;292:115–26.
[43] Li P, de Groot K, Kokubo T. Bioactive $Ca_{10}(PO_4)_6(OH)_2$–TiO_2composite coating prepared by sol–gel. J Sol–Gel Sci Technol 1996;7:27–34.
[44] Wilson R, Elliott J, Dowker S, Smith R. Reitveld structure refinement of precipitated carbonate apatite using neutron diffraction data. Biomaterials 2004;25:2205–13.
[45] El Feki H, Savariault J, Salah A, Jemal M. Sodium and carbonate distribution in substituted calcium hydroxyapatite. Solid State Sci 2000;2:577–86.